Magneto-optical and EPR transitions in Raman heterodyne spectroscopy

Marc Oliver Schweika-Kresimon, Jörg Gutschank, and Dieter Suter
Universität Dortmund, Fachbereich Physik, 44221 Dortmund, Germany
(Received 18 June 2002; published 30 October 2002)

Laser and microwave fields can be mixed in paramagnetic samples in a coherent Raman process. The radiation scattered in the forward direction contains frequency components at the sum and difference frequency. We consider the details of this scattering process in a static magnetic field, where two types of signals appear: magnetic-resonance transitions give rise to signals at fixed magnetic fields, independent of the laser frequency. Another set of resonances is determined by the optical transition frequencies. These resonances are particularly prominent in samples with narrow optical absorption lines. We derive a comprehensive theory that describes both contributions and compare it with experimental data from the *R* lines of ruby.

DOI: 10.1103/PhysRevA.66.043816 PACS number(s): 42.65.−k, 33.55.−b, 76.30.−v

I. INTRODUCTION

Coherent Raman scattering can be driven by external fields, such as alternating magnetic fields, whose frequencies are in the MHz to GHz range. The Raman field generated in this process propagates parallel to the incident laser field. If both fields are incident on a quadratic detector, the beat signal between them can be observed as a modulation with the same frequency as the driving radio frequency or microwave field. This combination of microwave-driven coherent Raman scattering with optical heterodyne detection is known as the Raman-heterodyne experiment [1–6]. It has been used for the optical detection of nuclear spin transitions [5–7] as well as for electron spin transitions [8–13]. The interaction of the optical and microwave field with the medium cannot only be described as a Raman process, it can also be considered as arising from a modulation of the absorption coefficient due to the magnetization precessing around the magnetic field [12,10]. The description is particularly well suited for comparison with different types of (static) magneto-optical effects.

This description is rather intuitive and provides an excellent basis for understanding the variation of optically detected electron paramagnetic resonance (EPR) spectra with the optical wavelength [13,11,12], provided the optical linewidth is large compared to the microwave frequency. However, if the width of the optical transitions is of the same order of magnitude as the microwave frequency or smaller, the analysis of the relevant processes in terms of a time-dependent absorption coefficient becomes invalid. To provide a better analysis of these cases, we describe the Raman scattering process by a perturbation expansion of the density operator. Comparing this analysis with experimental data from the *R* lines of ruby, (Cr^{3+}:Al_2O_3) we find excellent agreement for the vast majority of the observed features.

Figure 1 shows a typical Raman-heterodyne spectrum of ruby, measured with a laser whose frequency was tuned slightly higher than the resonance frequency for the R_2 transition. The setup measured the microwave-modulated light for left versus right circular polarization as a function of the static magnetic field B_x at a constant microwave frequency of $\nu_{MW}=14$ GHz.

As shown by the arrows in the figure, different types of resonance lines can be distinguished. The first three lines can be assigned to EPR transitions, which occur at the same position as conventional EPR transitions. The resonance at 1.4 T indicates that the field shifts the lowest ground-state level into resonance with the laser frequency, coupling it to the $2A(^2E)$ excited state. The two resonances at 1.1 and 1.7 T occur when the laser frequency plus or minus one of the two Raman sidebands become resonant with the same transition.

As we show below, these different transitions can be described consistently with second-order perturbation theory. The analysis that we present in the following section gives not only a correct description of such optically detected EPR

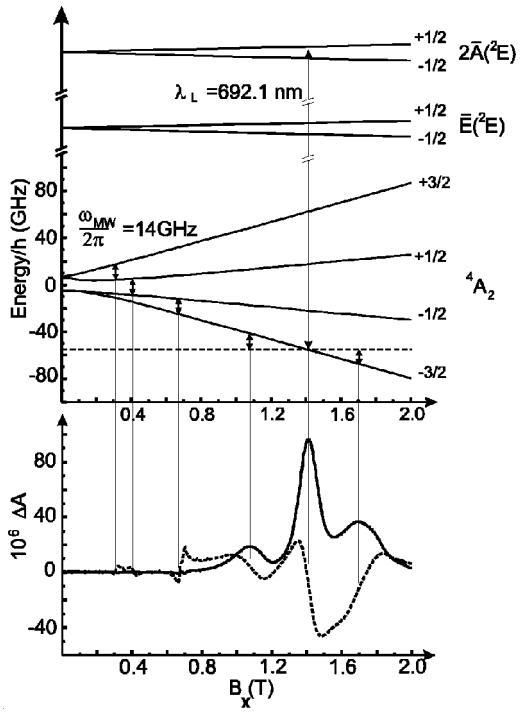

FIG. 1. Energy diagram and Raman-heterodyne spectrum of ruby, detected with a laser tuned close to the R_2 transition (solid line, absorption phase; broken line, dispersion phase). The absorption difference ΔA refers to the difference between the absorption of left and right circularly polarized light. The arrows indicate the transitions that give rise to the different resonance lines.

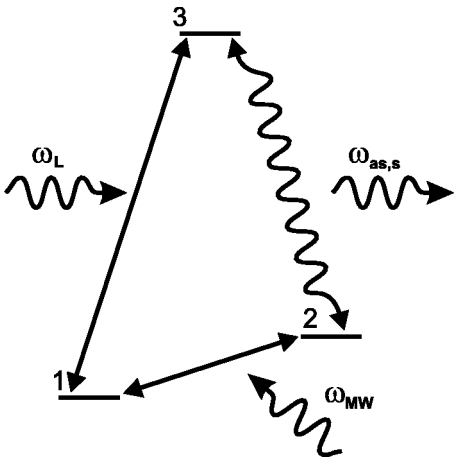

FIG. 2. Coherent Raman process in a three-level system.

spectra, but also correctly explains the dependence of these spectra on the optical wavelength; to our knowledge no such analysis has been attempted so far.

II. COHERENT RAMAN SCATTERING

The Raman-heterodyne experiment can be described as a superposition of coherent Raman scattering processes. While the ruby system consists of eight electronic states, the perturbation theory can be developed in terms of three levels, as shown in Fig. 2. Levels $|1\rangle$ and $|2\rangle$ are electronic ground states, while level $|3\rangle$ is an electronically excited state. The transition $|1\rangle \leftrightarrow |2\rangle$ is driven by a microwave field with the frequency ω_{MW}. The transition $|1\rangle \leftrightarrow |3\rangle$ is excited by laser light with the frequency ω_L.

The Hamiltonian of the relevant three level system is

$$\mathcal{H}=\mathcal{H}^0+V(t)=\begin{pmatrix} E_1 & V_{12}(t) & V_{13}(t) \\ V_{21}(t) & E_2 & 0 \\ V_{31}(t) & 0 & E_3 \end{pmatrix},$$

where $\mathcal{H}^0$ is the Hamiltonian of the undisturbed system with the energies $E_{1,2,3}$ of the three states. The elements V_{nm} of the perturbation potential $V(t)$ describe the interaction of the microwave and laser field,

$$V_{12}=-\vec{\mu}_{12}^{mag}\vec{B}_1(e^{-i\omega_{MW}t}+e^{i\omega_{MW}t}),$$

$$V_{13}=-\vec{\mu}_{13}^{el}(\vec{E}_L' e^{-i\omega_L t}+\vec{E}_L'^{*} e^{i\omega_L t}),$$

where $V_{nm}=V_{mn}^{*}$ and $\vec{\mu}_{12}^{mag}$ and $\vec{\mu}_{13}^{el}$ are the magnetic and electric dipole moments of the two transitions. The electric-field vector $\vec{E}_L'$ is complex to allow inclusion of arbitrary polarizations, while the microwave field $\vec{B}_1$ will be linearly polarized and therefore described by a real $\vec{B}_1$. In the following we will replace the product of the magnetic dipole moment and the microwave field by the real Rabi frequency $\omega_R=\vec{\mu}_{12}^{mag}\vec{B}_1/\hbar$.

To derive an expression for the Raman field generated by the mixing of the two driving fields, we use second-order perturbation theory for the density matrix of the system, in close analogy to similar derivations in nonlinear optics [14].

$$\dot{\rho}_{nm}^{(0)}=i\omega_{nm}\rho_{nm}^{(0)}-\gamma_{nm}(\rho_{nm}^{(0)}-\rho_{nm}^{eq}),$$

$$\dot{\rho}_{nm}^{(1)}=(i\omega_{nm}-\gamma_{nm})\rho_{nm}^{(1)}-\frac{i}{\hbar}[V(t),\rho^{(0)}]_{nm},$$

$$\dot{\rho}_{nm}^{(2)}=(i\omega_{nm}-\gamma_{nm})\rho_{nm}^{(2)}-\frac{i}{\hbar}[V(t),\rho^{(1)}]_{nm},$$

where γ_{nm} represents the relaxation rate of transition $|n\rangle \leftrightarrow |m\rangle$ ($\gamma_{nm}=\gamma_{mn}$) and $\omega_{nm}=(E_m-E_n)/\hbar$ the transition frequency.

Starting in thermal equilibrium, we obtain for the first-order density operator elements

$$\rho_{12}^{(1)}=\rho_{21}^{(1)*}=(\rho_{11}^{(0)}-\rho_{22}^{(0)})\omega_R\left[\frac{e^{-i\omega_{MW}t}}{\omega_{12}+\omega_{MW}+i\gamma_{12}}+\frac{e^{i\omega_{MW}t}}{\omega_{12}-\omega_{MW}+i\gamma_{12}}\right], \tag{1a}$$

$$\rho_{13}^{(1)}=\rho_{31}^{(1)*}=\frac{1}{\hbar}(\rho_{11}^{(0)}-\rho_{33}^{(0)})\left[\frac{\vec{\mu}_{13}^{el}\cdot\vec{E}_L' e^{-i\omega_L t}}{\omega_{13}+\omega_L+i\gamma_{13}}+\frac{\vec{\mu}_{13}^{el}\cdot\vec{E}'^{*}_L e^{i\omega_L t}}{\omega_{13}-\omega_L+i\gamma_{13}}\right]. \tag{1b}$$

Equation (1a) describes the spin coherence of the transition $|1\rangle \leftrightarrow |2\rangle$ induced by the microwave field. Equation (1b) describes the optical coherence in transition $|1\rangle \leftrightarrow |3\rangle$ induced by the laser field. We will neglect optically antiresonant terms such as the first term in the square brackets of Eq. (1b) in the following calculation, but will keep terms that are antiresonant with respect to the microwave frequency.

In second-order perturbation the spin and optical coherences are partly transferred to the third transition $|2\rangle \leftrightarrow |3\rangle$. We obtain the Raman coherence

$$\rho_{23}^{(2)}=\frac{\omega_R}{\hbar}\vec{\mu}_{13}^{el}\cdot\vec{E}'^{*}_L e^{i\omega_L t}[\Lambda_{123}(\omega_L,-\omega_{MW})e^{-i\omega_{MW}t}+\Lambda_{123}(\omega_L,\omega_{MW})e^{i\omega_{MW}t}], \tag{2}$$

with the two-dimensional triple-Lorentzian lines Λ_{123} defined as

$$\Lambda_{123}(\omega_L,\omega_{MW})=\frac{1}{\omega_{23}-\omega_L-\omega_{MW}+i\gamma_{23}}\times\left\{\frac{\rho_{33}^{(0)}-\rho_{11}^{(0)}}{\omega_{13}-\omega_L+i\gamma_{13}}+\frac{\rho_{22}^{(0)}-\rho_{11}^{(0)}}{\omega_{21}-\omega_{MW}+i\gamma_{21}}\right\}.$$

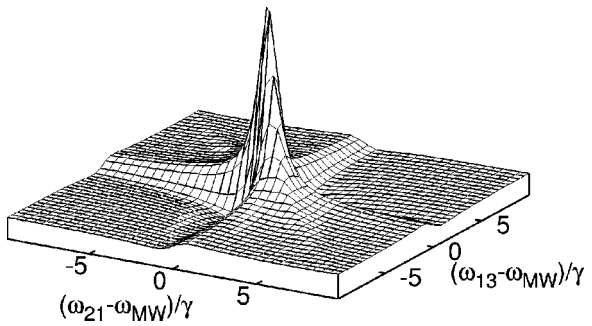

FIG. 3. Microwave and laser frequency dependence of $\Lambda_{123}(\omega_L,\omega_{MW})$ in arbitrary units (with $\gamma=\gamma_{12}=\gamma_{13}=\gamma_{23}$ and equal population differences). Only the real part is shown.

The first factor describes the resonant behavior of the Raman wave with respect to transition $|2\rangle\leftrightarrow|3\rangle$: It reaches a maximum when the frequency $\omega_{S,AS}=\omega_L+\omega_{MW}$ of the Raman field matches that of the transition frequency. The fractions in brackets describe the resonances of the laser and microwave with the transitions $|1\rangle\leftrightarrow|3\rangle$ and $|1\rangle\leftrightarrow|2\rangle$, respectively. Figures 3 and 4 depict the dependence of $\Lambda_{123}(\omega_L,\omega_{MW})$ on the microwave and laser frequencies. The magnetic resonances $(\omega_{21}-\omega_{MW}=0)$ and optical resonances $(\omega_{13}-\omega_L=0)$ appear on lines parallel to the frequency axes of the plot, while the Raman resonance appears along the diagonal $\omega_{23}-\omega_L-\omega_{MW}=0$.

The density operator element $\rho_{ij}^{(2)}$ corresponds to an optical polarization

$$\vec{P}^{(2)}=N(\rho_{23}^{(2)}\vec{\mu}_{32}^{el}+\rho_{32}^{(2)}\vec{\mu}_{23}^{el})$$
$$=(\vec{P}_{AS}e^{i(\vec{k}'_{AS}\cdot\vec{r}-\omega_{AS}t)}+\text{c.c.})+(\vec{P}_{S}e^{i(\vec{k}'_{S}\cdot\vec{r}-\omega_{S}t)}+\text{c.c.}), \tag{3}$$

with $\vec{k}'_{AS,S}=\vec{k}_L\pm\vec{k}_{MW}$ and N the number density. Since the rotating-wave approximation does not hold for the EPR transitions, we have to include Stokes as well as anti-Stokes components. The polarization (3) is the source of the Raman

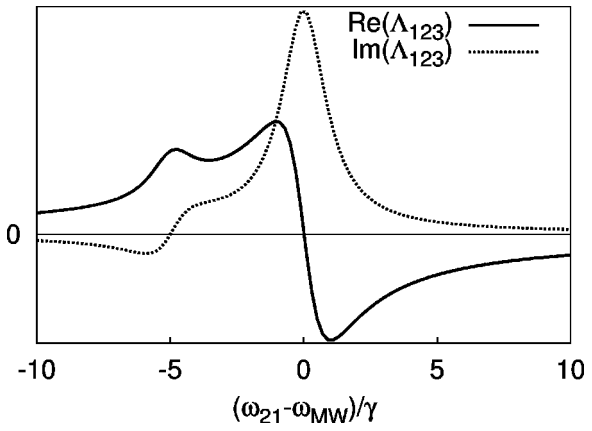

FIG. 4. Microwave frequency dependence of Λ_{123} at a normalized optical detuning $(\omega_{13}-\omega_L)/\gamma=5$. The resonance at $\omega_{21}-\omega_{MW})/\gamma=-5$ is the Raman resonance running diagonally through Fig. 3. The resonance at $\omega_{21}=0$ is the EPR transition.

waves. We write $\vec{E}_\alpha e^{i(\vec{k}_\alpha\cdot\vec{r}-\omega_\alpha t)}+\text{c.c.}$ with $\alpha=L,S,AS$ for the laser, Stokes, and anti-Stokes wave, respectively. The wave vectors $\vec{k}_{AS,S}$ of the Raman fields are functions of the Raman frequencies $\omega_{AS,S}=\omega_L\pm\omega_{MW}$. Since the sample is small compared to the wavelength of the microwave, the Raman wave is emitted in the forward direction. It remains weak compared to the laser field, allowing us to use the linear expansion

$$\vec{E}_\alpha=\frac{i\omega_\alpha^2\mu_0}{2k_\alpha}\vec{P}_\alpha L,$$

where L is the optical path length in the crystal. Using Eqs. (2) and (3), the two Raman waves become

$$E_\alpha=\frac{i\mu_0 LN\omega_R\omega_\alpha^2}{2\hbar k_\alpha}(\vec{\mu}_{31}^{el}\cdot\vec{E}_L)\vec{\mu}_{23}^{el}\Lambda_{123}^*(\omega_L,\pm\omega_{MW}),$$

where the plus sign is for the anti-Stokes field and the minus for the Stokes field.

III. HETERODYNE SIGNAL

The optical fields at the end of the crystal contain components with frequencies ω_L and $\omega_L\pm\omega_{MW}$. The Raman waves are polarized along $\vec{\mu}_{23}^{el}$ and $\vec{\mu}_{32}^{el}$, while the laser field is polarized along $\vec{E}_L$. When the signal is detected on a quadratic detector, it includes, besides a dominant dc component, components oscillating at the microwave frequency and its second harmonic. The first harmonic arises from beats between the laser field and each of the Raman sidebands, while the second harmonic is due to the beat between the two sidebands. The spatial components of the Raman field can be detected separately by projecting the (Raman plus laser) field onto a direction determined by a polarizer. Writing $\vec{E}^{(P)}$ for the fields behind the polarizer, the heterodyne signal at the microwave frequency becomes

$$I(\omega_{MW})^{(P)}=\text{Re}\Big[4\sqrt{\frac{\varepsilon_r\varepsilon_0}{\mu_0}}e^{-i\omega_{MW}t}(\vec{E}_{AS}^{(P)}\cdot\vec{E}_L^{*(P)}+\vec{E}_s^{*(P)}\cdot\vec{E}_L^{(P)})\Big]$$
$$=\text{Re}\Big[\frac{i2LN\omega_R\omega_L}{\hbar}e^{-i\omega_{MW}t}\{(\vec{\mu}_{31}^{el}\cdot\vec{E}_L)\times(\vec{\mu}_{23}^{el(P)}\cdot\vec{E}_L^{(P)*})\Lambda_{123}^*(\omega_L,\omega_{MW})-(\vec{\mu}_{13}^{el}\cdot\vec{E}_L^{*})\times(\vec{\mu}_{32}^{el(P)}\cdot\vec{E}_L^{(P)})\Lambda_{123}(\omega_L,-\omega_{MW})\}\Big], \tag{4}$$

where the approximation $\omega_{AS}\simeq\omega_S\simeq\omega_L$ was made for the amplitudes.

Experimental considerations often make it desirable to measure the difference between two signals. One way to do so is by modulating the polarization of the light incident on

TABLE I. The difference of the dot product $(\vec{\mu}_{31}^{el}\cdot\vec{E}_L)\cdot(\vec{\mu}_{23}^{el(P)}\cdot\vec{E}_L^{(P)*})$ divided by the square of the amplitude of the electrical field of the laser light E_0^2 calculated for some combinations of polarizations of the laser light and kinds of polarizing filters (For linearly polarized light, the angle between the direction of the magnetic field x and the linear polarization of the laser light is given in parentheses.)

	Polarization of laser light	
Filter	Linear (x,y)	Circular $(+,-)$
None	$\frac{1}{2}(\mu_{31}^{-}\mu_{23}^{-}+\mu_{31}^{+}\mu_{23}^{+})$	$\frac{1}{2}(\mu_{31}^{+}\mu_{23}^{-}-\mu_{31}^{-}\mu_{23}^{+})$
(0°)	$\frac{1}{4}(\mu_{31}^{+}+\mu_{31}^{-})(\mu_{23}^{+}+\mu_{23}^{-})$	$\frac{1}{4}(\mu_{31}^{+}-\mu_{31}^{-})(\mu_{23}^{+}+\mu_{23}^{-})$
(90°)	$\frac{1}{4}(\mu_{31}^{+}-\mu_{31}^{-})(\mu_{23}^{+}-\mu_{23}^{-})$	$\frac{1}{4}(\mu_{31}^{+}+\mu_{31}^{-})(\mu_{23}^{-}-\mu_{23}^{+})$
(45°)	$\frac{1}{4}(i\mu_{31}^{+}+\mu_{31}^{-})(\mu_{23}^{-}-i\mu_{23}^{+})$	$\frac{1}{4}(i\mu_{31}^{-}-\mu_{31}^{+})(i\mu_{23}^{+}-\mu_{23}^{-})$
Circ.	$\frac{1}{4}(\mu_{31}^{-}-i\mu_{31}^{+})(i\mu_{23}^{+}+\mu_{23}^{-})$	$\frac{1}{4}(\mu_{31}^{+}+i\mu_{31}^{-})(i\mu_{23}^{+}+\mu_{23}^{-})$

the sample in combination with phase sensitive detection. Here we will discuss two types of experiments. The first kind is the excitation with linearly polarized light. This provides a signal that is the difference of the intensities $I(\omega_{MW})^{x,y}$ for linearly polarized light oriented parallel (x) and perpendicular (y) to the external magnetic field. The second kind is the excitation with circularly polarized light. This results in a signal, which is the difference of the intensities $I(\omega_{MW})^{+,-}$ for left $(+)$ and right $(-)$ circularly polarized light. Additionally, it is possible to place polarizing filters between the sample and the photodetector. For these cases, the resulting signal is easily calculated from the general expression for a single polarization in Eq. (4). The possible signals are summarized in Table I for the cases of linear and circular polarization of the incident light and for five different analyzer settings. A circular basis was chosen for this summary.

Several of these optical setups (which are not linearly independent) can be seen as analog of standard magneto-optical experiments, such as magnetic circular dichroism (MCD) [15–18], magnetic circular birefringence (MCB, the dispersive aspect of the Faraday effect [19–21]), magnetic linear dichroism (MLD) [22], and magnetic linear birefringence (MLB, the dispersive aspect of the Cotton-Mouton effect [23,19–21]). In contrast to classical magneto-optical experiments here the magneto-optical effects are not induced by a static magnetization but by a magnetization oscillating at the microwave frequency. Typical experiments are the measurement of the *oscillating* MCD, MCB, MLD, or MLB. The corresponding polarizations of the incident laser beam and the setting of the polarization analyzer are summarized in Fig. 5.

IV. ENERGIES AND TRANSITION-MATRIX ELEMENTS

As a specific example, we consider the signal that is obtained when the laser is tuned close to the R lines of ruby. We choose the direction of propagation of the light parallel to the c axis to avoid effects from birefringence. We choose a coordinate system whose z axis is parallel to the c axis of the crystal, while the x axis lies along the static magnetic field. The magnetic component of the microwave field is also along the z axis.

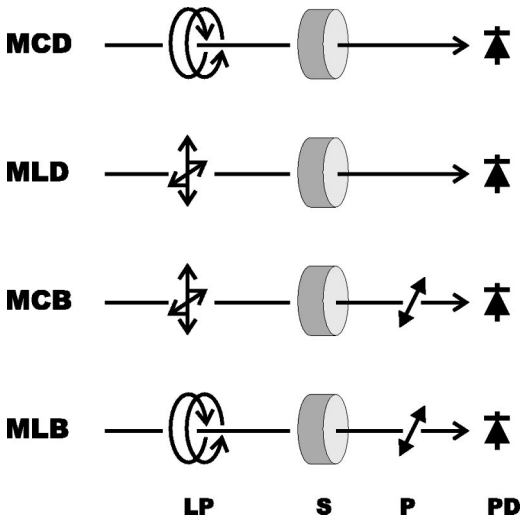

FIG. 5. Schematic optical setup for the detection of different magneto-optical effects (LP, polarization of the laser light; *S*, sample; *P*, polarizing filter 45°, PD, photo diode).

A. Ground state

The spin Hamiltonian for the ground state of ruby can be written as [24]

$$\mathcal{H}_g=g_x\mu_B B_x S_x+D\left\{S_z^2-\frac{1}{3}S(S+1)\right\},$$

with $g_x\mu_B B_x=\Omega_x$ the Larmor frequency and D the zero-field splitting. In the basis $\phi_{g;n}(n=1,2,3,4)=|M_S^z=-\frac{3}{2}\rangle$, $|M_S^z=-\frac{1}{2}\rangle,|M_S^z=\frac{1}{2}\rangle,|M_S^z=\frac{3}{2}\rangle$, the corresponding matrix representation is

$$\mathcal{H}_g=\begin{pmatrix} D & \frac{\sqrt{3}}{2}\Omega_x & 0 & 0 \\ \frac{\sqrt{3}}{2}\Omega_x & -D & \Omega_x & 0 \\ 0 & \Omega_x & -D & \frac{\sqrt{3}}{2}\Omega_x \\ 0 & 0 & \frac{\sqrt{3}}{2}\Omega_x & D \end{pmatrix}.$$

The eigenvalues are

$$E_{1,3}=-\frac{1}{2}\Omega_x\mp\sqrt{\Omega_x^2+D^2+\Omega_x D},$$

$$E_{2,4}=\frac{1}{2}\Omega_x\mp\sqrt{\Omega_x^2+D^2-\Omega_x D}.$$

We define the matrix $\mathbf{M}_g$ whose columns are the eigenvectors

$$\mathbf{M}_g=(\psi_{g;1},\psi_{g;2},\psi_{g;3},\psi_{g;4})=\frac{1}{\sqrt{2}}\begin{pmatrix} a_1 & a_2 & a_3 & a_4 \\ b_1 & b_2 & b_3 & b_4 \\ -b_1 & b_2 & -b_3 & b_4 \\ -a_1 & a_2 & -a_3 & a_4 \end{pmatrix},$$

with

$$a_i\equiv\frac{\sqrt{3}\Omega_x}{\sqrt{3\Omega_x^2+4(E_i-D)^2}},$$

$$b_i\equiv\frac{2(E_i-D)}{\sqrt{3\Omega_x^2+4(E_i-D)^2}}.$$

We use this matrix to obtain, e.g., the matrix representation of $\mathbf{S}_{z,g}$ and $\boldsymbol{\mu}_g^{z,mag}$ in the eigenbase of the Hamiltonian as

$$\boldsymbol{\mu}_g^{z,mag}=g_z\mu_B\mathbf{M}_g^T\cdot\mathbf{S}'_{z,g}\cdot\mathbf{M}_g,$$

where $\mathbf{S}'_{z,g}$ is the corresponding operator in the $\phi_{g;n}$ basis.

B. Excited states

The g tensor of the excited state is highly anisotropic. Here we assume that the crystal is oriented at an angle θ between the c axis and the z axis of the laboratory coordinate system. In the basis of the states $\phi_{e;5,6}=|^2E,u_+,-\frac{1}{2}\rangle$, $|^2E,u_-,\frac{1}{2}\rangle$ and $\phi_{e;7,8}=|^2E,u_-,-\frac{1}{2}\rangle,|^2E,u_+,\frac{1}{2}\rangle$ the Hamiltonian is

$$\mathcal{H}=\frac{1}{2}\begin{pmatrix} -\lambda-\Omega_z^{(1)} & \Omega_x^{(1)} & 0 & 0 \\ \Omega_x^{(1)} & -\lambda+\Omega_z^{(1)} & 0 & 0 \\ 0 & 0 & \lambda-\Omega_z^{(2)} & \Omega_x^{(2)} \\ 0 & 0 & \Omega_x^{(2)} & \lambda+\Omega_z^{(2)} \end{pmatrix},$$

with $\Omega_z^{(1,2)}=g_z^{(1,2)}\mu_B B_0\sin(\theta)$ and $\Omega_x^{(1,2)}=g_x^{(1,2)}\mu_B B_0\cos(\theta)$, where $g_{x,z}^{(1,2)}$ are the splitting factors of the excited state and λ the separation between the two R lines. The corresponding eigenstates $\psi_{e;n}$ $(n=5,6,7,8)$ are

$$\mathbf{M}_e=(\psi_{e;5},\psi_{e;6},\psi_{e;7},\psi_{e;8})=\frac{1}{\sqrt{2}}\begin{pmatrix} a_+^{(1)} & a_-^{(1)} & 0 & 0 \\ -a_-^{(1)} & a_+^{(1)} & 0 & 0 \\ 0 & 0 & a_+^{(2)} & a_-^{(1)} \\ 0 & 0 & -a_-^{(2)} & a_+^{(2)} \end{pmatrix},$$

with

$$a_\pm^{(i)}=\sqrt{\frac{1}{2}\left(1\pm\frac{\Omega_z^{(i)}}{\sqrt{\Omega_x^{(i)2}+\Omega_z^{(i)2}}}\right)}.$$

The corresponding energies E_n are

$$E_{5,6}=E(R_1)\mp\frac{1}{2}\sqrt{\Omega_x^{(1)2}+\Omega_z^{(1)2}},$$

$$E_{7,8}=E(R_2)\mp\frac{1}{2}\sqrt{\Omega_x^{(2)2}+\Omega_z^{(2)2}}.$$

The magnetic transition matrix $\boldsymbol{\mu}_e^{z,mag}$ for the excited states is

$$\boldsymbol{\mu}_e^{z,mag}=\mathbf{M}_e^T\boldsymbol{\mu}'^{mag}\mathbf{M}_e,$$

with the matrix

$$\boldsymbol{\mu}'^{mag}=\frac{1}{2}\mu_B\begin{pmatrix} g_z^{(1)}\cos(\theta) & -g_x^{(1)}\sin(\theta) & 0 & 0 \\ -g_x^{(1)}\sin(\theta) & g_z^{(1)}\cos(\theta) & 0 & 0 \\ 0 & 0 & g_z^{(2)}\cos(\theta) & -g_x^{(2)}\sin(\theta) \\ 0 & 0 & -g_x^{(2)}\sin(\theta) & g_z^{(1)}\cos(\theta) \end{pmatrix}.$$

C. Transition-matrix elements

The transition matrix elements for the optical excitation of the R lines were calculated by Sugano and Tanabe [25] and by Henderson and Imbusch [26]. In the eigenbase the matrix elements for circularly polarized light are

$$\boldsymbol{\mu}^\pm=\langle\psi_e|\mu|\psi_g\rangle=\mathbf{M}_e^T\boldsymbol{\mu}'^\pm\mathbf{M}_g,$$

with

$$\boldsymbol{\mu}'^{+} = \langle \phi_e | \mu^+ | \phi_g \rangle = C^+ \begin{pmatrix} 0 & \frac{2}{3} & 0 & 0 \\ 0 & 0 & 0 & -\sqrt{\frac{2}{3}} \\ 0 & 0 & -\frac{\sqrt{2}}{3} & 0 \\ 0 & 0 & \frac{2}{3} & 0 \end{pmatrix},$$

$$\boldsymbol{\mu}'^{-} = \langle \phi_e | \mu^- | \phi_g \rangle = C^- \begin{pmatrix} -\sqrt{\frac{2}{3}} & 0 & 0 & 0 \\ 0 & 0 & -\frac{2}{3} & 0 \\ 0 & -\frac{2}{3} & 0 & 0 \\ 0 & -\frac{\sqrt{2}}{3} & 0 & 0 \end{pmatrix}.$$

The prefactors $C^{\pm}$ are functions of the energy splitting between the states ^2E and $^4T_2$, the transition strength of the U band and the single-electron spin-orbit matrix element [25].

V. SIGNAL IN MCD CONFIGURATION

We consider first the Raman-heterodyne experiment where the polarization of the incident light is modulated between left and right circular and no analyzer is used before detection. An expression for the signal is given by Eq. (4) and the difference expressions from Table I,

$$S^{MCD} = \frac{iLNE_0^2 \omega_R \omega_L}{\hbar} \cdot [\{(\mu_{13}^{-*}\mu_{23}^{-} - \mu_{13}^{+*}\mu_{23}^{+}) \times \Lambda_{123}^*(\omega_L, \omega_{MW})\} - \{(\mu_{13}^{-}\mu_{23}^{-*} - \mu_{13}^{+}\mu_{23}^{+*}) \times \Lambda_{123}(\omega_L, -\omega_{MW})\}], \quad (5)$$

where the frequency and magnetic-field dependence is expressed by the triple-Lorentzian lines Λ_{ijk}. The prefactors are proportional to the products $\mu_{13}^{\pm}\mu_{23}^{\pm *}$ of the optical and magnetic transition-matrix elements. In Eq. (5) only the optical transition-matrix elements $\mu_{ij}^{\pm}$ contain complex expressions in the proportionality factors $C^{\pm}$. For the trigonal field of ruby the absolute values $|C^+| = |C^-| \equiv C$ are equal, therefore we can write the product

$$\mu_{13}^{\pm}\mu_{23}^{\pm *} = \mu_{13}^{\pm *}\mu_{23}^{\pm} = |C|^2 m_{13}^{\pm} m_{23}^{\pm}$$

in terms of the real matrix elements $m_{ij}^{\pm}$. With this notation, the signal becomes

$$S^{MCD} = \frac{iLN|C|^2 E_0^2 \omega_L \omega_R}{\hbar} (m_{13}^{+} m_{23}^{+} - m_{13}^{-} m_{23}^{-}) \times \{\Lambda_{123}(\omega_L, -\omega_{MW}) - \Lambda_{123}^*(\omega_L, \omega_{MW})\}.$$

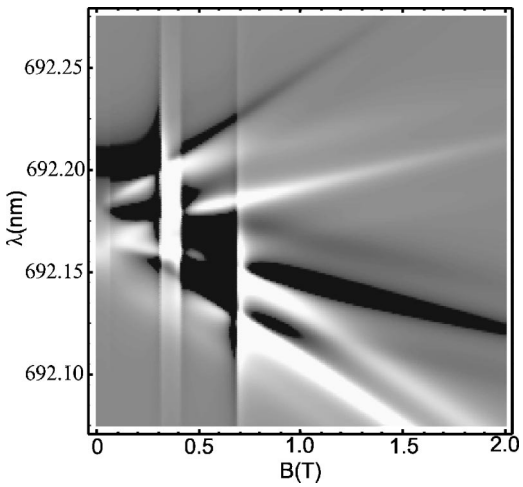

FIG. 6. Density plot of the absorption component of the Raman-heterodyne signal as a function of the magnetic-field strength and the laser frequency in the vicinity of the R_2 line.

To apply these results to a multilevel system like ruby, we sum over all three-level subsystems of the eight-level system.

VI. SPECTRA

The experimental setup used to obtain these spectra has been described elsewhere [27]. The experimental data were obtained from a ruby crystal (concentration of Cr:Al 5×10^{-4}) of a cylindrical shape (5 mm diameter $\times$2 mm thick), which was kept in liquid helium at a temperature of 1.8 K. The power of the laser light was about 5 mW, while the microwave power was 150 mW at a frequency of 13.7 GHz. The spectra were taken by scanning the magnetic field and keeping the wavelength of the laser fixed. 32 spectra for the R_2 line and 28 for the R_1 line were recorded at different wavelengths, and a simultaneous fit of all spectra yielded a consistent set of parameters (Tables III and IV).

A. Overview

Figure 6 shows an overview of the calculated absorption-phase component of the Raman-heterodyne signal as a function of the magnetic field and the laser frequency close to the R_2 line. This representation clearly shows the different contributions to the signal: the magnetic resonance transitions occur at constant magnetic fields, independent of the laser frequency. In this two-dimensional representation, they appear as vertical stripes at 0.3 T, 0.4 T, and 0.7 T. The optical and magneto-optical resonance lines follow the splitting of the Zeeman levels of the ground state because the splitting of the excited states is much smaller; they can be seen as diagonal lines in Fig. 6.

If the laser wavelength is close to the optical transition frequency, the different signal contributions overlap. At larger detunings, i.e., for wavelengths $\lambda > 692.225$ nm or $\lambda < 692.125$ nm, the magnetic resonances are separated from the optical and magneto-optical resonances, as can be seen by the examples of the spectrum at 692.081 nm in Fig. 7.

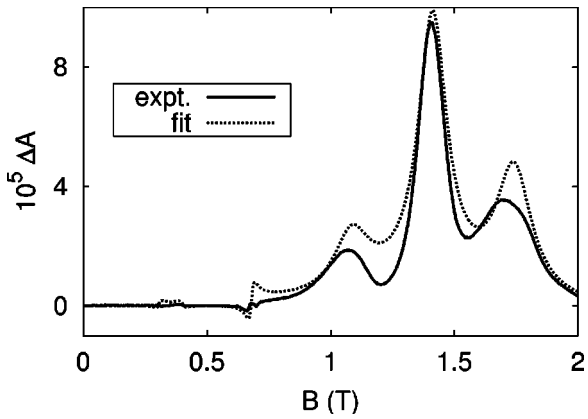

FIG. 7. An example of a fitted experimental spectrum at 692.081 nm (simulated spectrum, dashed line; experimental spectrum, straight line).

While the EPR transitions are at 0.3, 0.4, and 0.7 T, the optical transition $\psi_1 \leftrightarrow \psi_{7,8}$ appears at 1.4 T, with the corresponding magneto-optical transitions at 1.1 T and 1.7 T.

The dependence of the Raman-heterodyne spectra on the optical wavelength λ has been shown previously to provide very useful information on the orientation of optical transition moments in anisotropic biological systems [13]. The wavelength dependence is also correctly explained by the theory presented here. Figure 8 depicts the signal amplitudes for the magnetic resonance at 0.3 T as an example. The agreement is better with the experimental data for the R_2 line then for R_1.

In order to demonstrate how much the separate three-level subsystems contribute to the overall signal, Fig. 9 shows these contributions for the spectrum at a wavelength of 692.081 nm. The main contributions at this wavelength are due to the subsystems $\psi_1\psi_2\psi_7$ and $\psi_1\psi_2\psi_8$, which best fulfill the optical resonance condition at this wavelength. The subsystems $\psi_2\psi_3\psi_{7,8}$ and $\psi_3\psi_4\psi_7$ give rise to the two EPR lines at 0.4 T and 0.3 T, respectively. They are farther from optical resonance but fulfill the magnetic resonance condition. The *V*-type subsystem $\psi_1\psi_7\psi_8$ reduces the amplitude of the Stokes magneto-optical line at 1.1 T and increases the amplitude of the optical line and the anti-Stokes magneto-optical line at 1.4 T and 1.7 T, respectively, if the splitting factors $g_z^{(1,2)}$ are chosen as they are given in the literature.

Stokes and anti-Stokes fields contribute to the Raman signal with different phase and amplitude and it has been shown

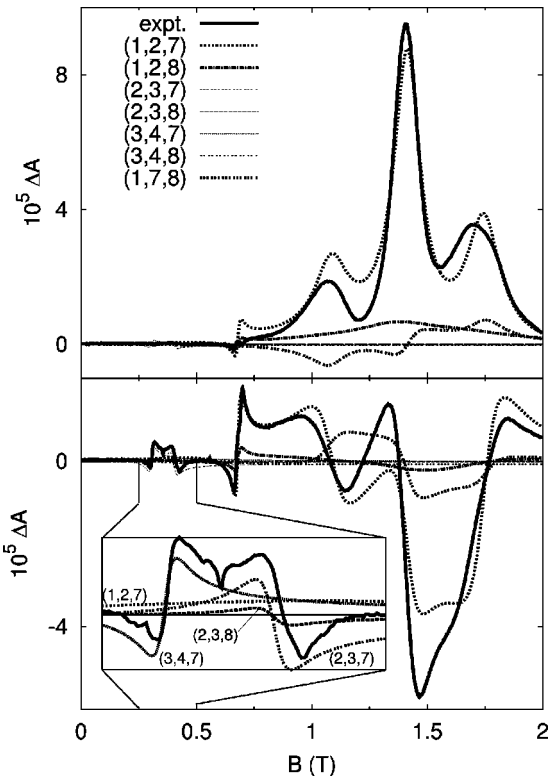

FIG. 9. Contributions of the different three-level subsystems to the absorption (top) and dispersion (bottom) phase of the spectrum at 692.081 nm. Solid line, measured spectrum, (k,l,m), contribution of the subsystem of the three states ψ_k, ψ_l, and ψ_m to the fit. The inset shows the main contributions of the dispersion phase between 0.25 T and 0.5 T.

that the separate contributions can cancel partly [6,28–31]. Figure 10 depicts the contributions of the Stokes and anti-Stokes-Raman waves to the spectrum at 692.081 nm. In the magneto-optical part of the spectrum, each wave contributes to the center resonance and to one of the two sidebands. In the EPR part of the spectrum, the Stokes and anti-Stokes waves contribute to all resonances of the dispersion signal with different sign and similar amplitude. The resultant amplitude of the magnetic resonance lines is therefore significantly smaller than its two Raman contributions. To increase the signal of the magnetic resonances it might be advantageous to detect Stokes- and anti-Stokes contributions separately [7].

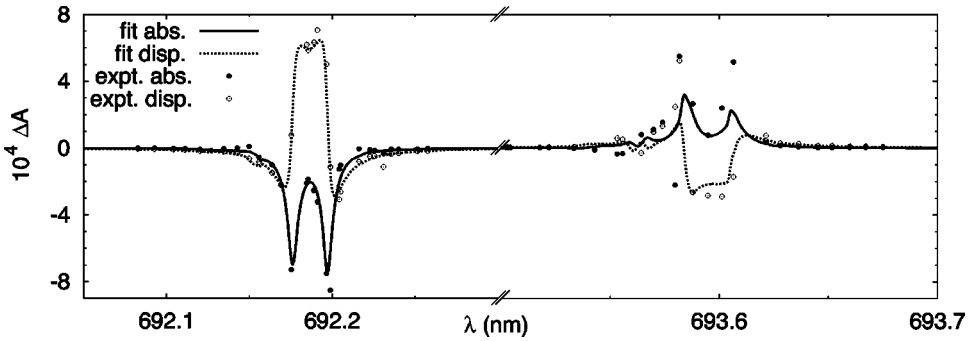

FIG. 8. Wavelength dependence of the magnetic resonance at 0.3 T. Experimental amplitudes are shown as circles, fits as lines. (solid line, circle: absorption; dotted line, open circle: dispersion).

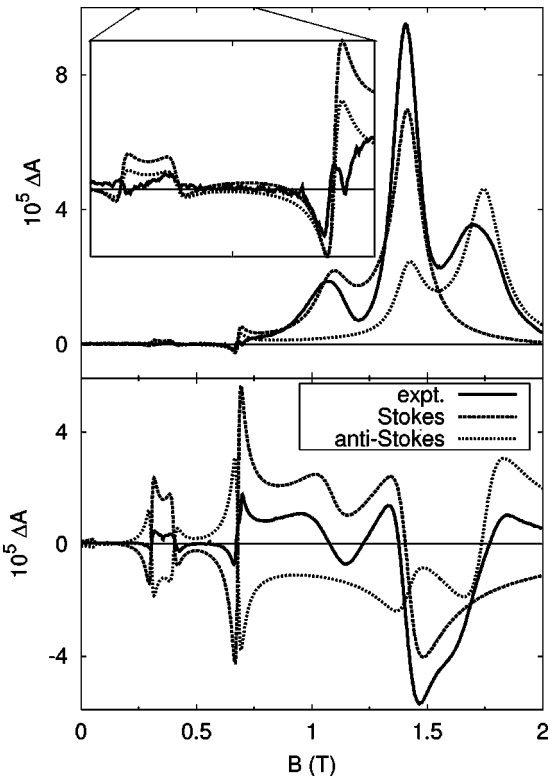

FIG. 10. Contributions of the Stokes and anti-Stokes-Raman waves to the absorption (top) and dispersion (bottom) phases of the spectrum at 692.081 nm. The inset shows the main contributions of the absorption phase between 0.25 T and 0.75 T.

B. Line shapes

The dispersion part of the magnetic resonance signal is well represented by the theoretical expression, but the experimental absorption signal is significantly smaller than the theoretical value. The dependence of the signal on the microwave power clearly shows that this is due to saturation. While the theoretical spectra were calculated with the Boltzmann distribution of the ground-state populations, which corresponds to population differences of the order of 10%, saturation reduces these population differences. As in conventional EPR, saturation effects are stronger in the absorption signal than in the dispersion component [32].

We take these effects into account in the theoretical spectra by setting the population difference in the ground states $(\rho_{22}^{(0)}-\rho_{11}^{(0)})$ to zero for the absorption component. The dispersion component was multiplied by a scaling factor f_s, and a saturation contribution was added to the width of the EPR line.

From the theoretical analysis, we expect that the optical transition and the two magneto-optical transitions should have the same line shape. Experimentally, we find that the magnetooptical lines are significantly broader. We take this into account in the simulated spectrum by scaling the dephasing rate of the Raman transition with a factor f_b. With these modifications, the triple-Lorentzian line-shape function is (for numerical values of the fit parameters see Tables III and IV),

$$\Lambda_{123}(\omega_L,\omega_{MW})=\frac{1}{\omega_{23}-\omega_L-\omega_{MW}+if_b\gamma_{23}}\times\left\{\frac{\rho_{33}^{(0)}-\rho_{11}^{(0)}}{\omega_{13}-\omega_L+i\gamma_{13}}+f_s\frac{(\rho_{22}^{(0)}-\rho_{11}^{(0)})(\omega_{21}-\omega_{MW})}{(\omega_{21}-\omega_{MW})^2+(\gamma_{21})^2}\right\}.$$

TABLE II. Literature values of the splitting factors, energies, and zero-field splitting.

Parameter	Experimental value	Theory [a]
$g_x(^4A_2)$	1.9867 ± 0.0006 [b]	1.9890
g_z	1.9840 ± 0.0006 [b]	1.9789
$\delta=2D$	-0.38 cm^{-1} [b] ($\triangleq-11.447$ GHz)	$(-)0.16$ cm^{-1}
$g_x^{(1)}$	<0.06 [c]	0.004
$g_x^{(2)}$	<0.5 [d]	0.04
$g_z^{(1)}$	2.44 ± 0.08 [c]	2.59
$g_z^{(2)}$	1.48 ± 0.08 [e]	1.23
$E(R_1)$	14 418 cm^{-1} [e]	14 588 cm^{-1}
$E(R_2)$	14 447 cm^{-1} [e]	14 626 cm^{-1}

[a]Reference [34].
[b]Reference [33].
[c]Reference [35]. (The sign convention of the splitting factors g_z of the excited states differs here from the cited literature.)
[d]Reference [36].
[e]Reference [37].

TABLE III. Results of fit parameters.

	R_1	R_2
$\lvert C\rvert(10^{-30}$ C m)	1.075	1.162
f_s	1.461	1.318
f_b	1.538	1.253
$\gamma^{mag}(10^9$ s$^{-1})$	1.868	2.165
$g_x^{(i),expt}$	0.1335	0.0394

C. Splitting factors

The literature values of the splitting factors, energies, and zero-field splitting are listed in Table II. The results of the fitted parameters are summarized in Tables III and IV. These parameter values have been used to calculate the signal. In our experiments the crystal has not been perfectly oriented

TABLE IV. Optical linewidth γ_{nm} in units of 10^9 s^{-1}.

$n\backslash m$	1	2	3	4
5	16.473	10.244	17.690	56.972
6	13.263	11.046	17.040	5.244
7	15.973	10.961	15.111	9.614
8	11.376	5.525	15.535	23.370

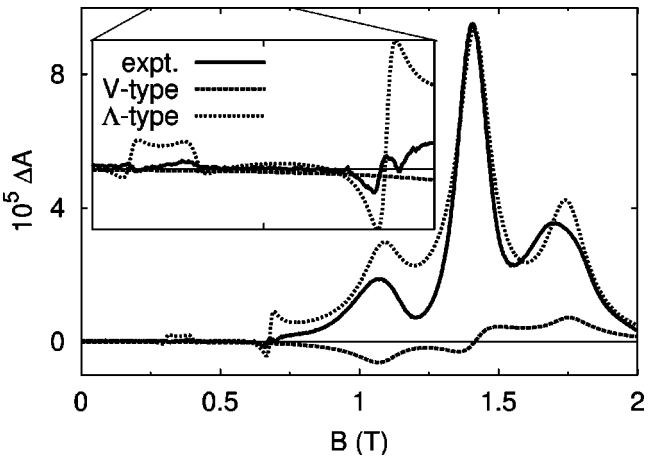

FIG. 11. Contributions of V- and Λ-type configurations to the absorption phase of the spectrum at 692.081 nm. The inset depicts the detail between 0.25 T and 0.75 T.

($\theta = 4.93°$). Thus the strong anisotropy of the g tensor of the excited states causes a slightly bigger splitting than expected in perfect orientation,

$$g_x^{(1),expt} \approx 0.1,$$

$$g_x^{(2),expt} \approx 0.04.$$

While most of the signal is due to Λ-type three-level subsystems, the optical and magneto-optical resonance lines also include contributions from V-type configurations. Figure 11 compares the two types of contributions. The amplitude of the V-type configurations depends on the splitting factors $g_z^{(1,2)}$, which determine the magnetic transition-matrix elements of the excited states. The contribution is relatively small for the R_2-line spectra, but is significant for the shape of the R_1-line spectra. It is experimentally quite difficult to measure the sign of the splitting factors of excited states with other techniques, but their absolute value has been measured precisely (Table II).

D. Optical configurations

The biggest Raman signals are obtained with the MCD-optical configuration discussed above. The other possible configurations, which are listed in Table I, yield signals whose information is complementary to that obtained with the MCD configuration. The spectra depicted in Fig. 12 have been taken with an MCD, MLD, and MCB configuration according to Fig. 5.

In contrast to the MCD spectra, the MLD spectra depend on the relative phase of the products C^+C^{-*} and C^-C^{+*}. Good agreement between the simulated and experimental spectra is achieved with the relation $C^+C^{-*} = -C^-C^{+*}$. In principle, the spectra measured in an MCB configuration should provide the absolute phase of C^+ and C^-, because these spectra have contributions from both the MLD configuration scaling with C^+C^{-*} and C^-C^{+*} and the MCD configuration scaling with $i|C|^2$. However, the MCD part of the signal is much larger than the MLD part, so that the resulting uncertainties for the phase of $C^{\pm}$ are quite large.

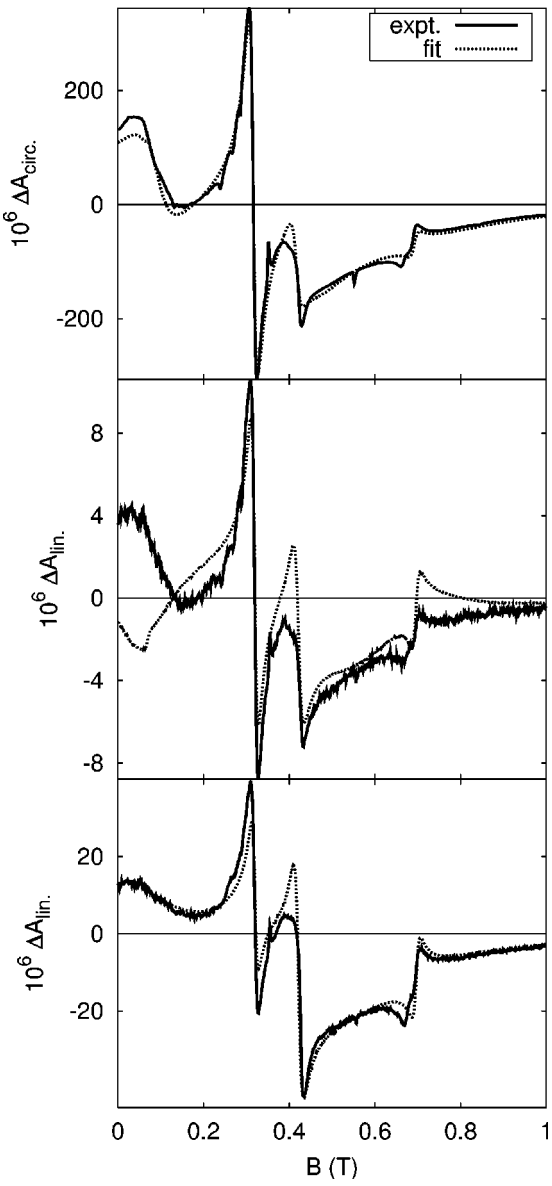

FIG. 12. Comparison of spectra (dispersion phases at 692.20 nm) taken with MCD, MLD, and MCB configurations.

E. Additional resonances

While the signal contributions discussed up to now explain most of the features of the experimental spectra, we found some additional resonance lines under specific experimental conditions.

The first kind of additional lines are absorption type lines appearing at 0.28 T, 0.35 T, 0.55 T, and 0.84 T. The lines at 0.28 T and 0.84 T are small and only observable in a narrow range of experimental parameters. The lines at 0.35 T and 0.55 T appear at almost any wavelength where the signal amplitude close to these lines is sufficiently high. As depicted in Fig. 13 these lines can be assigned to double quantum transitions ($\Delta E = 2\hbar\omega_{MW}$) between the ground-state components. Double quantum transitions are not excited in second-order perturbation theory, since the matrix elements of the magnetic dipole operator vanish for these transitions.

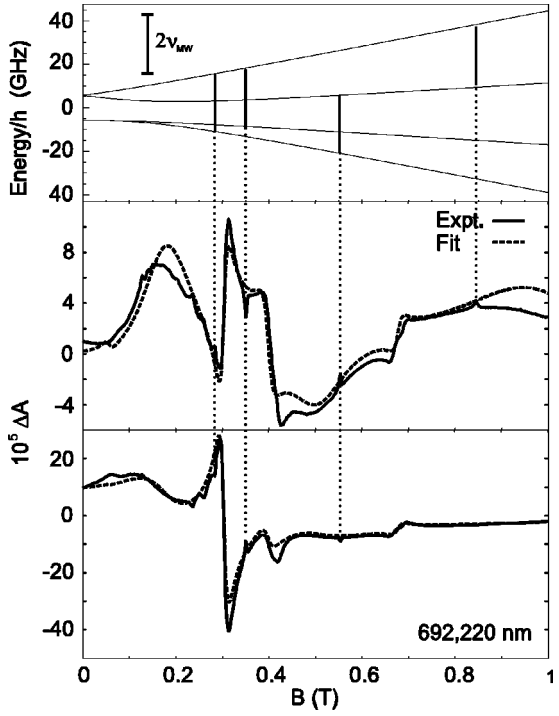

FIG. 13. Appearance of double quantum transition resonances demonstrated by spectra at 692.220 nm [absorption (top) and dispersion (bottom) phase].

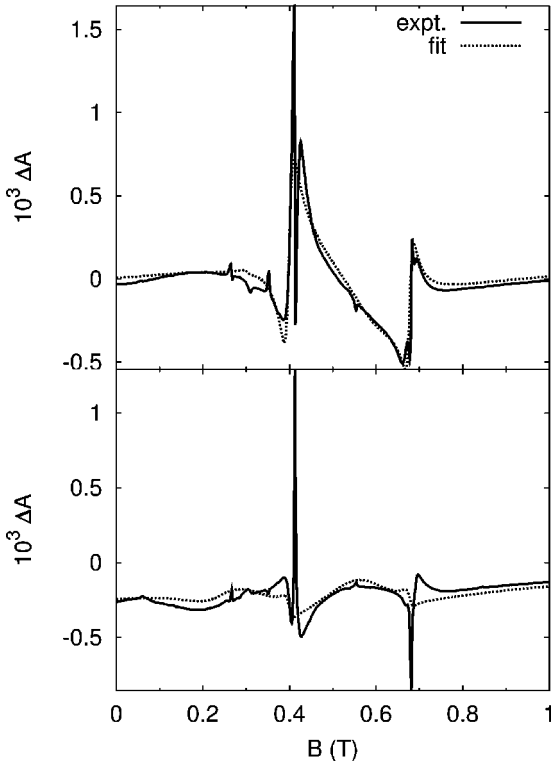

FIG. 14. Narrow lines at the EPR resonances at 693.578 nm [absorption (top) and dispersion (bottom) phase].

However, they can be described in an analogous manner by extending the perturbation expansion to higher order.

The second kind of additional lines are very narrow and appear under EPR-resonance conditions at wavelengths close to 693.580 nm, as depicted in Fig. 14. At other wavelengths just small deformations in the dispersion line shape hint that additional lines with smaller line width contribute to the signal. A possible explanation for the appearance of these lines is that they are due to Cr ion pairs [38,39]. For such pairs, the relaxation rates tend to be much shorter than for isolated ions. They would therefore exhibit reduced saturation, particularly for the absorption component, and the linewidth would be reduced. The energies of the optically excited states are shifted by the interaction of the Cr ions. The optical resonance condition for these ion pairs is therefore different from those of the isolated ions and the signal maximum appears at a different wavelength.

VII. CONCLUSION

The main features of Raman-heterodyne spectra of transition-metal ions in a static magnetic field contain two main contributions. One contribution is due to EPR transitions and appears at a constant magnetic field, independent of the laser frequency, while the second signal contribution is associated with (magneto-)optical transitions and shifts with the laser frequency. Depending on the width of the optical resonance lines and the laser frequency detuning, one or the other of these contributions may dominate the spectrum.

Both signal contributions can be described quantitatively by second-order perturbation theory. Using the well-characterized *R* lines of ruby as a test system, we have obtained excellent agreement between experimental and theoretical spectra over a wide range of parameters.

Compared to other treatments [5–7,12], the theory yields the signal for arbitrary optical configurations. It is applicable to high spin systems, such as ruby, and it can be applied to narrow optical resonance lines.

ACKNOWLEDGMENTS

We wish to thank S. J. Bingham and B. Börger-Enkisch for establishing this experimental technique in our group and A. J. Thomson who provided a part of the experimental equipment. We gratefully acknowledge the support of the Deutsche Forschungsgemeinschaft (DFG).

[1] E. Garmire, F. Pandarese, and C. Townes, Phys. Rev. Lett. **11**, 160 (1963).
[2] J.A. Giordmaine and W. Kaiser, Phys. Rev. **144**, 676 (1966).
[3] R. Brewer and E. Hahn, Phys. Rev. A **8**, 464 (1973).
[4] M. Levenson, Phys. Today **30**(**5**), 44 (1977).
[5] N.C. Wong, E.S. Kintzer, J. Mlynek, R.G. DeVoe, and R.G. Brewer, Phys. Rev. B **28**, 4993 (1983).
[6] T. Blasberg and D. Suter, Phys. Rev. B **51**, 12 439 (1995).

[7] R. Neuhaus, M.J. Sellars, S.J. Bingham, and D. Suter, Phys. Rev. A **58**, 4961 (1998).
[8] K. Holliday, X.-F. He, P.T.H. Fisk, and N.B. Manson, Opt. Lett. **15**, 983 (1990).
[9] S.J. Bingham, D. Suter, A. Schweiger, and A.J. Thomson, Chem. Phys. Lett. **266**, 543 (1997).
[10] B. Börger, S.J. Bingham, J. Gutschank, M.O. Schweika, D. Suter, and A.J. Thomson, J. Chem. Phys. **111**, 8565 (1999).
[11] S.J. Bingham, B. Börger, J. Gutschank, D. Suter, and A.J. Thomson, JBIC, J. Biol. Inorg. Chem. **5**, 30 (2000).
[12] S.J. Bingham, J. Gutschank, B. Börger, D. Suter, and A.J. Thomson, J. Chem. Phys. **113**, 4331 (2000).
[13] B. Börger, J. Gutschank, D. Suter, A.J. Thomson, and S.J. Bingham, J. Am. Chem. Soc. **123**, 2334 (2001).
[14] R. W. Boyd, *Nonlinear Optics* (Academic Press, San Diego, 1992).
[15] S. B. Piepho and P. N. Schatz, *Group Theory in Spectroscopy with Applications to Magnetic Circular Dichroism* (Wiley, New York, 1983).
[16] P.J. Stephens, Adv. Chem. Phys. **35**, 197 (1976).
[17] J. C. Sutherland, Methods Enzymol. **246**, 110 (1995).
[18] A. J. Thomson, M. R. Cheesman, and S. J. George, Methods Enzymol. **226**, 199 (1993).
[19] M. Born, *Optik* (Springer-Verlag, Berlin, 1972).
[20] J.-P. Pérez, *Optik* (Spektrum Verlag, Heidelberg, 1996).
[21] Y. R. Shen, *The Principles of Nonlinear Optics* (Wiley, New York, 1984).
[22] M. Kreglewski and M. Vala, J. Chem. Phys. **74**, 5411 (1981).
[23] A.D. Buckingham and J.A. Pople, Proc. Phys. Soc. London, Sect. B **69**, 1133 (1956).
[24] A. Abragam and B. Bleaney, *Electron Paramagnetic Resonance of Transition Ions* (Oxford University Press, London, 1970).
[25] S. Sugano and Y. Tanabe, J. Phys. Soc. Jpn. **13**, 880 (1958).
[26] B. Henderson and G. F. Imbusch, *Optical Spectroscopy of Inorganic Solids* (Oxford University Press, Oxford, 1989).
[27] S.J. Bingham, B. Börger, D. Suter, and A.J. Thomson, Rev. Sci. Instrum. **69**, 3403 (1998).
[28] E.S. Kintzer, M. Mitsunaga, and R.G. Brewer, Phys. Rev. B **31**, 6958 (1985).
[29] M. Mitsunaga, E.S. Kintzer, and R.G. Brewer, Phys. Rev. B **31**, 6947 (1985).
[30] D.R. Taylor, Opt. Commun. **52**, 204 (1984).
[31] M. Mitsunaga, E.S. Kintzer, and R.G. Brewer, Phys. Rev. Lett. **52**, 1484 (1984).
[32] A.M. Portis, Phys. Rev. **91**, 1071 (1953).
[33] A. Manenkov and A. Prokhorov, Sov. Phys. JETP **1**, 611 (1955).
[34] S. Sugano and M. Peter, Phys. Rev. **122**, 381 (1961).
[35] S. Geschwind, R.J. Collins, and A.L. Schawlow, Phys. Rev. Lett. **3**, 545 (1959).
[36] K. Aoyagi, A. Misu, and S. Sugano, J. Phys. Soc. Jpn. **18**, 1448 (1963).
[37] S. Sugano and I. Tsujikawa, J. Phys. Soc. Jpn. **13**, 899 (1958).
[38] K. Sato, M. Hirai, and T. Tamaki, J. Phys. Soc. Jpn. **61**, 10 (1992).
[39] A. Schawlow, D. L. Wood, and A. M. Clogston, Phys. Rev. Lett. **3**, 271 (1959).